Acta Materialia 246 (2023) 118721

Contents lists available at ScienceDirect

Acta Materialia

journal homepage: www.elsevier.com/locate/actamat

Nanoscale mapping of point defect concentrations with 4D-STEM

Sean H. Mills [a,b], Steven E. Zeltmann [a], Peter Ercius [b], Aaron A. Kohnert [c], Blas P. Uberuaga [c], Andrew M. Minor [a,b,*]

[a] Department of Materials Science and Engineering, University of California, Berkeley, CA 94720, USA
[b] National Center for Electron Microscopy, Molecular Foundry, Lawrence Berkeley National Laboratory, Berkeley, CA 94720, USA
[c] Materials Science and Technology Division, Los Alamos National Laboratory, Los Alamos, NM 87545, USA

ARTICLE INFO

Keywords:
High-resolution electron microscopy (HREM)
Irradiated metals
Vacancies
Thermal cycling
Four-dimensional scanning electron microscopy (4D-STEM)

ABSTRACT

Vacancies are missing atoms in a crystalline material, and occur both at equilibrium (varying with temperature) and out of equilibrium such as when crystalline materials are damaged with radiation or corrosion. While we know of their importance, particularly regarding diffusive mechanisms, it is not straightforward to experimentally measure their concentration or to visualize them directly. Traditionally, measurements such as positron annihilation spectroscopy and to some degree X-ray diffraction can measure average concentrations, but generally lack the ability to visualize or quantify a heterogenous concentration of vacancies that can occur at the level of individual defects and microstructural features. Here, we present a method to map vacancy concentrations and their distribution using local lattice parameter measurements with a high-resolution electron microscope. Our method utilizes a Au thin film as a model to demonstrate the method via four-dimensional scanning transmission electron microscopy (4D-STEM) by correlating the differences between changes in lattice parameter and the volumetric thermal expansion during in situ heating experiments. The vacancy mapping methodology is also applied to non-equilibrium defects accumulated in pure Al via knock-on electron beam irradiation. Our method demonstrates the ability to map point defect concentrations in heterogeneous systems in situ with nanometer spatial resolution. The result is a technique that can provide direct measurements of vacancy concentrations at the level of individual defects in studies of materials in and out of equilibrium.

1. Introduction

A wide variety of important questions involving the thermophysical and structural properties of materials are tied to the equilibrium concentration of point defects. Vacancies are the simplest form of defects and are fundamental features shared by a variety of microstructural processes such as solidification, short range ordering in a crystal lattice, plastic deformation, and irradiation. The formation of point defects in solids was initially theorized by Frenkel et al. [1], who postulated that atoms become more mobile at elevated temperatures and overcome constraints imposed by the surrounding lattice. Atoms move to interstitial sites leaving behind a vacancy, which together are termed a 'Frenkel pair'. The Wagner-Schottky model describes how vacancies remain in an otherwise perfect crystal when interstitial atoms leave their initial lattice positions to occupy free sites such as sample surfaces and other crystal imperfections [2]. Modern theories suggest defects are directly created at these imperfections. Regardless of the source, the result is an equilibrium vacancy concentration that is required for plasticity mechanisms such as dislocation climb [3,4] and diffusional creep [5].

In transient conditions such as electrochemical cycling (eg- Li-ion battery cathodes or corrosion reactions in metals) or in extreme environments such as nuclear reactors, materials can evolve vacancy (and other point defect) concentrations substantially beyond what is considered a thermodynamic equilibrium. In these cases, ephemeral and heterogeneous vacancy concentrations impact mechanisms that degrade a material's performance [6]. In these situations, the rate of point defect formation and migration are critical to determining the evolution of damage and rate of corrosion; however, the trends associated with varied temperature and irradiation dose are not intuitive, and a mechanistic understanding of the associated thermodynamics and kinetics remains poorly understood [7]. Therefore, a method for measuring and spatially resolving point defects such as vacancies is essential for the fundamental understanding of material behavior under complex

* Corresponding author at: One Cyclotron Road, MS 72, Berkeley, CA 94720, USA.
E-mail address: aminor@berkeley.edu (A.M. Minor).

https://doi.org/10.1016/j.actamat.2023.118721
Received 7 October 2022; Received in revised form 23 November 2022; Accepted 19 January 2023
Available online 20 January 2023

damage modes.

Higher vacancy concentrations at elevated temperatures lead to an expansion in the sample volume, becoming most prominent as the temperature approaches the melting point of the crystal [8]. Therefore, the concentration of point defects can be effectively determined by measuring the difference between the volume expansion (or measured length if considering isotropic expansion) and the increase in the lattice parameter of a crystal. Foundational measurements by Simmons and Balluffi [9–11] benchmarked this technique in bulk Al, Au, and Cu crystalline bar specimens by using optical dilatometry (to measure length change) and X-ray diffraction (XRD) (to measure lattice change).

Until recently, capabilities for directly determining the concentration of vacancies by way of measuring lattice parameter change have been limited to bulk techniques such as XRD [10] as noted previously or positron annihilation spectroscopy (PAS) [12], where vacancies act as traps for positrons by which the vacancy accumulation can be quantified. Generally, these techniques provide volume-averaged properties (though recent depth-resolved PAS capabilities can provide some depth resolution [13,14]). Recent developments in four-dimensional scanning transmission electron microscopy (4D-STEM) using high-speed direct electron detectors [15,16] coupled with high resolution STEM now provide an opportunity for mapping lattice parameters at ~10 – 20 s time resolution with high precision [17] and over a relatively wide field of view [18]. Nano-beam electron diffraction (NBED) analysis of strain is a more straightforward alternative to conventional high resolution TEM techniques such as convergent beam electron diffraction (CBED), HR-TEM and dark-field holography as the local precision is not dependent on matching to simulations or measuring atomic column positions. [15,19]. The interatomic spacing is inversely related to the spacing of diffraction disks and is capable of measuring nearly any crystalline sample, orientation, and field of view [15]. This offers the possibility of correlating defect content with microstructural features in metallic materials at nanoscale spatial resolution. 4D-STEM has been recently used to map stoichiometry [20] and compositional changes [21,22], but has not been used to map primary vacancy concentrations where there is no change in chemical composition. Utilizing Au films in thermal equilibrium and irradiated Al out of equilibrium, we demonstrate a state-of-the-art nanoscale point defect mapping technique and discuss fundamental vacancy-related mechanisms with respect to our experimental observations.

2. Methods

2.1. Materials and sample preparation

Au thin films were deposited on single crystal NaCl substrates using a custom thermal evaporator (NCEM, Molecular Foundry, LBNL). Bulk material (99.99% pure) was carefully weighed and placed in an Al_2O_3 coated Mo crucible to minimize contamination of the evaporated product. The vacuum chamber was pumped down to a pressure of $< 10^{-6}$ mbar. High purity optical grade single crystal NaCl was selected as an evaporation substrate due to its ability to grow smooth epitaxial thin films in the (100) orientation [23] as is shown in the high resolution annular dark field scanning transmission electron microscopy (HR-ADF-STEM) image in Fig. 1a. The substrate was cleaved into ~ 5 mm × 5 mm × 2 mm coupons and heated to 400 °C for the duration of the evaporation. Power supply to the crucible was held at constant voltage (5 V) while the current was slowly increased to allow for gradual heating of the crucible until evaporation transpired at 105 – 120 mA. Using a thickness monitor (Gatan) the deposition rate was held at ~ 1 – 5 Å/second to achieve a steady deposition of ~ 50 nm. Once the Au was fully evaporated from the boat (indicated by near-zero measured change in thickness), the sample on salt substrate was held at 400 °C for 15 min before slow cooling to 17 °C. To remove the thin films from NaCl, the coupons were sectioned with a razor blade and partially submerged in DI water until the substrate fully dissolved, leaving the film suspended on the surface of the water. A looped wire tool was used to transfer the thin film via a water droplet to the ultra-thin carbon membrane section of a Protochips Fusion Select™ MEMS device (amorphous holey carbon film). The film was carefully positioned over the exposed holey grid section of the membrane without contacting the electrodes on either side. The MEMS device was tested for a proper connection in the Protochips double tilt heating and biasing holder prior to the in-situ experiment. The detected shift in peak temperature positions enables measurement of relative temperatures. The lattice parameter of (4.070 Å) 17 °C is selected as a reference for which the diffraction patterns and elevated temperature measurements are compared. Furthermore, the electrothermal e-chip used in these experiments has been calibrated by Protochips to maintain a 5% temperature accuracy and uniform heating across the entire heating membrane. The accuracy of this temperature measurement has been demonstrated to a statistical precision as low as 2.8 K on similar MEMS-based electrothermal e-chips is well documented

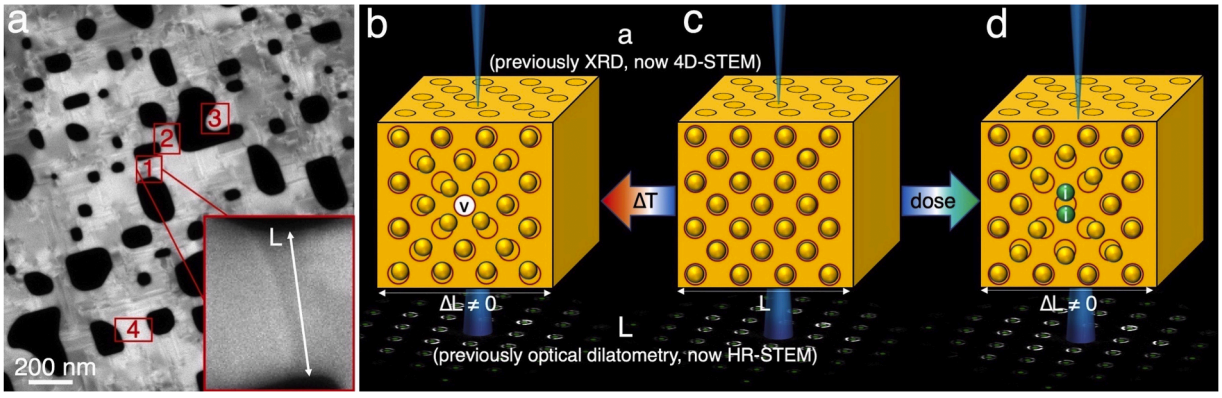

Fig. 1. Schematic of 4D-STEM point defect mapping. (a) Length measurements were conducted on HAADF-STEM images of most narrow point of bridge-like ligament sections (red inset) corresponding to the sample locations R1 – R4 where 4D-STEM measurements were taken in situ at each heating step. Lattice parameter measurement was derived from the average lattice parameters from collected 4D-STEM strain maps of the probed sample region. (b-d) Schematic illustrations of a nano-beam electron beam converged on a Au thin film. (c) Pure crystal at room temperature which is free of defects with a geometric dimension L. The d-spacing and lattice parameter are measured from a diffraction pattern collected for each scan position. (b) High temperature crystal containing a vacancy defect (white "v") where the surrounding Au atoms are displaced in tension with respect to their unstrained lattice configuration (red circles). (d) Electron-beam irradiated crystal containing a split self-interstitial (green "i") and here the surrounding Au atoms are displaced in compression with respect to their unstrained lattice configuration (red circles). The change in lattice parameter and d-spacing are measured via HR-STEM and 4D-STEM, respectively. (For interpretation of the references to colour in this figure legend, the reader is referred to the web version of this article.)

and the error (± 20 K) is not significantly affected by relative changes in temperature [24]. Moreover, there is a known temperature gradient across these types of devices, however the probed sample regions are suspended over a single aperture, and it is assumed that the sample is unconstrained by contact with the MEMS chip.

2.2. In-situ heating and nano-diffraction electron microscopy

Au thin films were studied due to their ultra-thin geometry for HR-STEM characterization. Au is an ideal material choice for study at varied temperatures as it does not oxidize and is unaffected by air, water and nearly all acids. Moreover, the interrogated region was inspected for chemical impurities and second phase particles that would otherwise contribute to systematic error during the thermal cycling experiment. It's capacity to produce and retain point defects at high temperatures is well reported [25]. The design of the present experiment closely follows the differential thermal expansion method of measuring concentrations of point defects where thermally generated lattice-vacancy-type defects that compensate an equal quantity of atoms can be measured [10]. The lattice parameter (measured by X-ray diffraction previously, but now by 4D-STEM [15]) and linear dilation (measured by filar micrometer previously, but now by STEM imaging) was studied at various elevated temperatures (Fig 1b). Measurement of additional atomic sites (vacancy production) as a function of increasing temperature is reproduced in situ on suspended Au thin films through implementation of a Protochips™ double-tilt Fusion Select holder set-up to control sample heating with minimal drift.

4D-STEM measurements were conducted on a Thermofisher Scientific ThemIS image corrected microscope at 300 kV. NBED data was collected using a Gatan K2-IS (2k × 2k) detector at 400 frames per second. Each dataset contains a set of electron diffraction patterns (Fig. 2e-h) taken at each scan position with a ~ 1 nm probe step size. Approximately 80 × 80 scan positions were recorded from each region with a dwell time of 0.0025 s per frame. A convergence angle of 3.20 milli-radians, spot size of 8, and diffraction pixel size of 0.16 $\mathring{A}^{-1}$ was used in micro-probe lens configuration to accommodate the inherent trade-off between real-space resolution and strain resolution [15]. A custom 40 μm patterned "bullseye" circular probe forming aperture was used to enhance the accuracy of 4D-STEM strain analysis by facilitating the identification of the center of diffraction discs by correcting for inconsistencies in the diffraction data such as dynamical scattering, inelastic scattering and shot noise and, thereby improving the robustness of peak finding of the diffraction disk centers [17]. The bullseye probes provide an advantage to uneven disk illumination with reported up to 30 times improvement in thin specimens at high electron counts. The "blooming" effect around the edges of the probe that are prone to form by dynamical effects is corrected in a similar approach to Sobel filtering in CBED patterns by adding many edges that are defined by the template. Experimental error in the NBED measurement of strain was explored by determining the cross-validation error, or the error associated with the length of the reciprocal lattice vector for a given experimental NBED pattern [17]. The use of bullseye condenser apertures allows for precise dentification of disk centers, and cross-validation error is minimized to < 1% for every 1% change in strain. This is critical when measuring lattice variations in samples where fluctuations in thickness, tilt, and defects may be a factor [17]. The cross-validation error maps provided in Fig. 3 indicate an average error of 0.45% for ± 1% change in strain, or ± 0.0002 Å error for ±0.041 Å change in lattice parameter for diffraction measurements of the Fig. 3b thermally cycled Au and Fig. 3e irradiated Al, respectively. The distribution of error for each are shown in Fig. 3c,f. The 4D-STEM data was machine and software binned to 512 × 512 pixels to increase the signal to noise ratio before computational analysis. Additional 4D-STEM calibration data sets were acquired using a polycrystalline Al standard to correct for systematic errors such as scanning drift, elliptical distortion, and STEM rotation, which is necessary to attain highly accurate lattice parameter measurements. Data processing was performed using strain mapping scripts provided in the open source py4DSTEM software package [16].

HR-ADF-STEM images (Fig. 2a-d) were acquired contingent with the 4D-STEM scans at each temperature step per heating cycle and used for careful measurement of ligament sections indicated by the red boxes. Fiji image processing software was used to acquire 20 measurements at

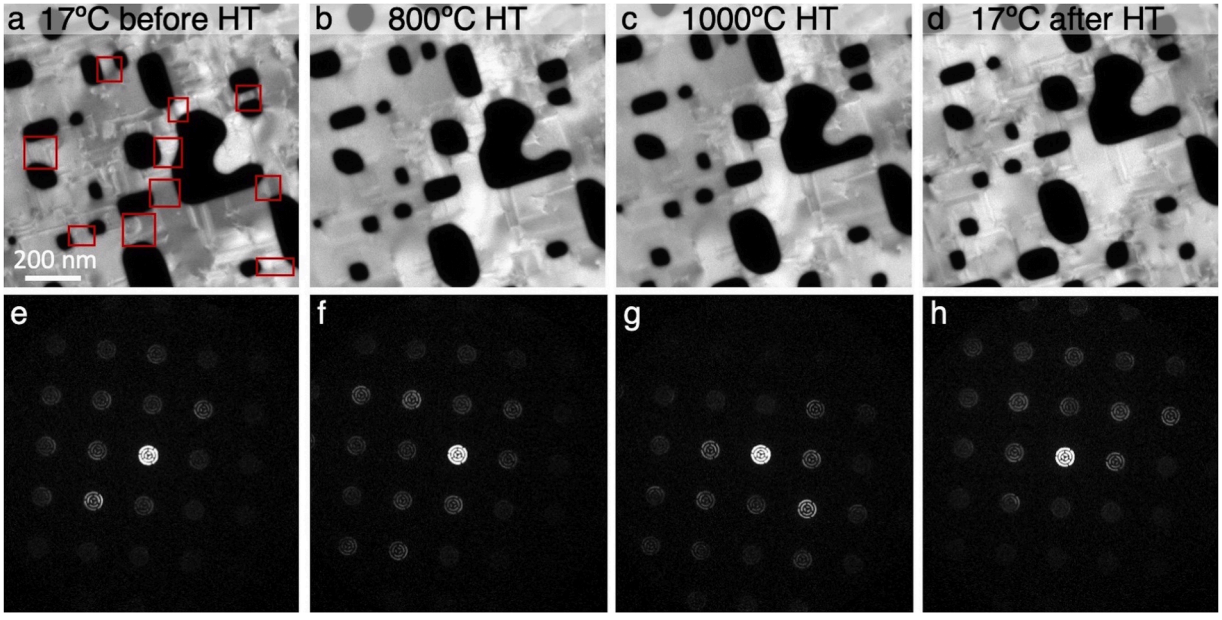

Fig. 2. Example test data for sample length and lattice parameter measurement. High resolution ADF-STEM images of Au thin film sample (a) 17 °C before heat treatment; (b) 800 °C during heat treatment; (c) 1000 °C during heat treatment; (d) 17 °C after rapidly cooling. Sample regions (red boxes in (a)) were used for linear dilation measurement at each ligament and compared to the pristine sample. 4D-STEM patterns taken along $(001)_{Au}$ zone axis were collected at (e) 17 °C before heat treatment; (f) 800 °C during heat treatment; (g) 1000 °C during heat treatment; (h) 17 °C after rapidly cooling. (e-f) were calibrated for systematic errors using a polycrystalline Al diffraction standard and used for measuring lattice parameter change compared to the pristine sample. (For interpretation of the references to colour in this figure legend, the reader is referred to the web version of this article.)

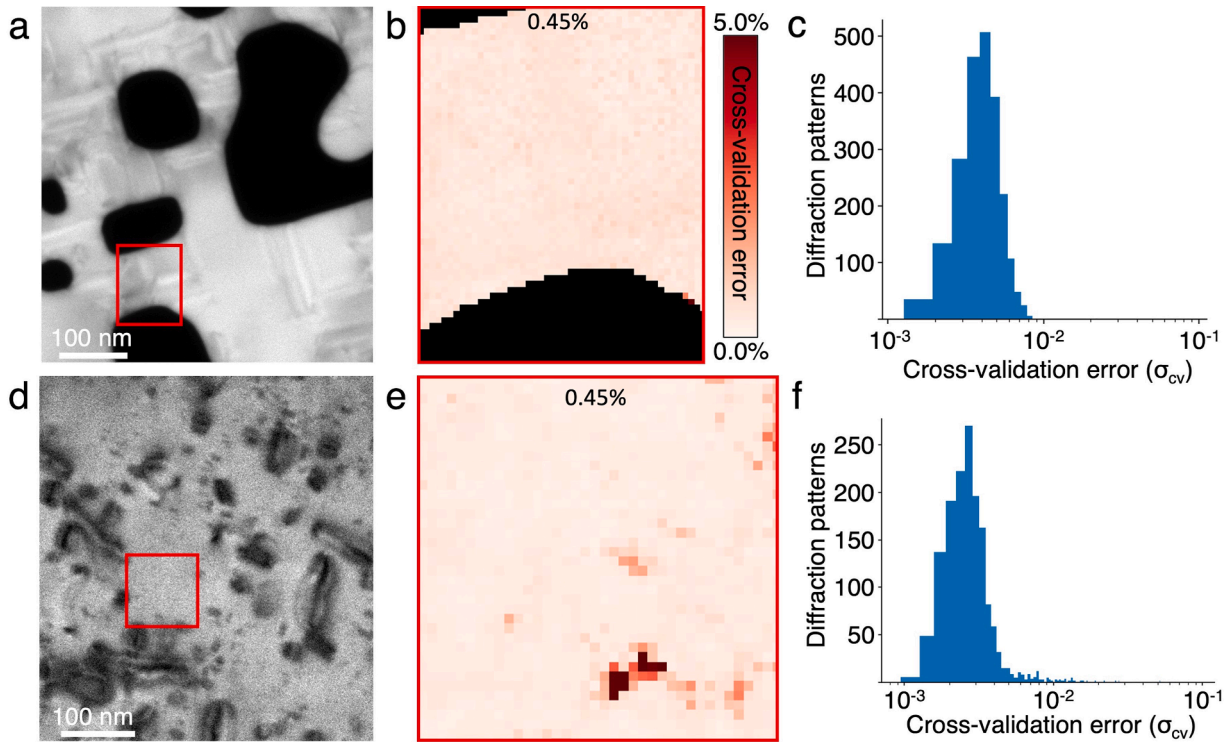

Fig. 3. Cross-validation error of 4D-STEM measurements for (a-c) Au sample and (d-f) Al sample. (a,d) High resolution ADF-STEM images with red boxes indicating where 4D-STEM scans were taken. (b, e) A lattice was fitted to half of the identified diffraction disks and the error associated with the remaining half of the disks for each individual pattern is mapped for each dataset. The label on each map indicates the mean error over the field of view. (e, f) Plots of the distribution of cross-validation error for the total number of diffraction patterns for Au and Al, respectively. (For interpretation of the references to colour in this figure legend, the reader is referred to the web version of this article.)

each ligament which were averaged to determine the linear dilation of the ligament (compared to the measured mean dimension of the pristine ligament condition). The standard deviation at each temperature step is provided based on the variation between individual measurements with respect to the mean dilation using the sampling size of 20 measurements. We can estimate with some degree of certainty, the thickness effect on changes in orientation. If we consider 1° of tilt between the sample and the incident beam, the net change on the visible ligament dimension would be ~ 0.5 nm. Considering the observable change to the diffraction patterns (Fig. 2e-f) are at or below 1° of tilt over the full heating cycle, the volumetric error associated with the sample tilt is approximately at the single pixel resolution of the measurement.

The light green colored regions in Fig. 4 indicate lattice positions where contraction is occurring (less than or equal to the reference region (red box)). Conversely, darker blue colored regions indicate lattice positions where expansion is occurring. The average lattice parameter is taken from the distribution of measurements at each scan position across selected sample regions. Lattice expansion ($\Delta a/a = 12.43 \times 10^{-3}(0.17)$) and linear dilation ($\Delta L/L = 12.79 \times 10^{-3}(0.21)$) measured at 800 °C corresponds to a net added concentration in vacancy sites of 1.08×10^{-4}. The maximum lattice expansion ($16.18 \times 10^{-3}(0.66)$) and linear dilation ($17.08 \times 10^{-3}(0.79)$) measured at 1000 °C correspond to a net added concentration in vacancy sites of 2.91×10^{-4}. The distribution of the lattice parameter measurement is provided as a standard deviation of the measurement of lattice expansion measurement for individual scan positions with respect to the average lattice expansion using the sampling size of ~ 1600 diffraction patterns per 4D-STEM scan. Documented TEM approaches, such as convergent beam electron diffraction (CBED), have resulted in highly accurate lattice parameter measurement (< 10 nm spatial resolution) by using dynamical simulations to allow for precise determination of accelerating voltage [26]. One study applied parallel beam electron diffraction (PBED) to measure lattice parameter change in relation to thermal expansion where temperature was estimated to ± 2.8 K [24]. Furthermore, these determinations of lattice parameter through bulk or in situ TEM, and their usefulness in mapping vacancies, is either an average and/or limited to the interaction volume of the beam at a single position and generally lacks the ability to visualize or quantify a heterogenous concentration of vacancies.

In pure Au, the binding energy is relatively high for the vacancies to overcome the migration energy at ambient temperatures (30 – 125 °C, $E_B = 0.71 \pm 0.03$ eV [27]). At moderate temperatures (400 – 500 °C) this threshold reaches approximately 0.3 eV, where the mutual attraction between neighboring atoms is reduced, and minimal vacancies form in a pristine lattice [28,29]. However, there is evidence of retained defects after heating/quenching and the measured concentration of accumulated vacancies ranges from $1.5 \times 10^{-6} - 5.0 \times 10^{-5}$ [28,29]. Approaching the melting point of most pure metals, the concentration of thermally generated vacancy defects reaches a peak ($10^{-4} - 10^{-3}$). These defects, dispersed evenly through an otherwise pristine lattice, promote a nonlinear effect on the specific heat and thermal expansion approaching the melting point in Au (600 – 1063 °C) [8,30]. Moreover, non-equilibrium vacancy concentrations can accumulate in thin films, nano-wires and nano-porous structures during repeated material degradation processes such as heating/quenching [2], mechanical deformation [31], and irradiation damage [32]. In the pristine condition (before heating experiment) the thin film contained pre-existing defects such as holes, twins, stacking faults and nanoscale voids. These features (in addition to neighboring free surfaces) have been known to attract excess vacancies and grow and is a common behavior in thin films [25]. There is not a significant change in the morphology and distribution of these defects during the thermal cycling. It is assumed that vacancies remain homogenously distributed throughout the film and reach equilibrium concentration within microseconds each elevated temperature

measurement.

Aggregated thermal effects like surface diffusion, residual stress, etc. are potential complications for extracting point defect density in the complex thin film geometry. By measuring these effects at multiple conditions, we can correct for them. As a basis for this correction, the lattice expansion and linear dilation defined as $\frac{\Delta a}{a} = (-\lambda)x_v + \varepsilon^p_{rel} + \varepsilon_{res} + \int \alpha(T)dt$ and $\frac{\Delta L}{L} = (1+\lambda)x_v + \varepsilon^p_{rel} + \varepsilon_{res} + \int \alpha(T)dt$, respectively. ε^p_{rel} is creep relaxation, ε_{res} is residual strain, and $\int \alpha(T)dt$ is thermal expansion as a function of temperature and time. Using the experimental lattice expansion and linear dilation measurements taken after the 30-day room temperature hold (assuming $x_v = 0$ and $\int \alpha(T)dt = 0$), the net effect of the creep relaxation and residual strain are determined. These are subtracted from linear dilation (ΔL/L) at the other room temperature measurements to normalize the defect concentration (ΔN/N).

2.3. Knock-on electron beam damage and in situ nano-diffraction electron microscopy

4D-STEM measurements were conducted on an FEI TitanX microscope equipped for high-angle STEM tomography and operating at 300 kV. Nano-diffraction data was collected using a Gatan Orius 830 (2k × 2k) detector capable of collecting 30 frames per second. Each dataset contains a stack of convergent beam electron diffraction (CBED) patterns taken at each scan position with maximum resolution equivalent to 1.6 nm probe size. Approximately 50 × 50 frame scan regions were recorded with a dwell time of 0.01 s per frame. A custom 70 μm patterned "bullseye" circular C2 aperture was used to greatly enhance the accuracy of 4D-STEM strain analysis by facilitating the identification of the center of diffraction discs [17]. A convergence angle of 2.7 milli-radians, spot size 10, and camera length 195 mm was used in micro-probe lens configuration. With a measured screen current of 300 pA in this configuration, the total sum of electrons incident in a region of the sample, commonly known as the fluence (total dose), was determined at 67,100 electrons$Å^{-2}$ per 4D-STEM scan [33]. After each scan, an HR-ADF-STEM image was acquired. The 4D-STEM data was machine and software binned to 512 × 512 pixels to increase the signal to noise ratio before computational analysis. Data processing and image analysis were performed using strain mapping scripts provided in the open source py4DSTEM software package [16].

Applying the same general methodology to this unique microstructure benchmarks the use of 4D-STEM nano-diffraction and HR-STEM imaging for measuring defect concentrations and their spatial distribution which has not been possible with prior established techniques (XRD, PAS, etc.). Moreover, high-voltage electron microscopy (HVEM) has been used to interrogate 2D MoS_2 crystals by observing the growth speed of a dislocation loop through surface heating by the incident electron beam [34]. This indirect approach to extract vacancy migration energies was feasible through careful sample selection and microscope parameters coupled with utilization of established phenomenological dislocation loop models. Dislocation loops are known to form in pure metals under certain beam energies, defects can form prior to nucleation of a dislocation loop in a pristine microstructure. Heavier elements, such as Au have a relatively high threshold energy (1320 keV) and are therefore beyond the incident beam energy (300 keV accelerating voltage) in modern transmission electron microscopes that could be used to produce permanent defects. A model metal sample was necessary to showcase a mix of mono-vacancies and non-equilibrium vacancy-type defect clusters are present. Al has a much lower threshold energy (180 keV) that is well within the energy range of a condensed STEM probe, so it was selected for the knock-on damage experiment.

Electron beam damage is complex in nature and may activate a variety of mechanisms to accommodate this damage. Knock-on damage is considered in this case as a simplified assessment for producing point defects and the total dose is accepted as a first order approximation of accumulated damage. There are other likely contributions to the irradiation damage such as displaced atoms sputtered from the sample surface or knocking into vacancies present in the lattice [35], that coincide with the formation of surface voids [36]. Moreover, prior reporting shows that long term vacancy retention (> 10 h) is noticeably suppressed in a void dense environment [25]. Therefore, changing morphology and density of pre-existing defects is directly linked to the quenching and room temperature annealing results. An approach to determining the extent of voids on this measurement would be to compare electron-beam damage in a void filled sample (He-ion irradiated) and a pristine sample. Other avenues to investigate include dose fractionation and dose rate as both are reported to control damage and, in consequence, the morphology of the irradiated zone [33,37], and may be considered for future study. Further, this nanobeam diffraction analysis is typically an average measurement, however the beam converges at the upper surface and the measurement may be weighted as such. In contrast, the electron beam damage is likely through the sample thickness, and particularly at the exit surface. Investigations by way of tomography analysis would be of particular importance to determine the precise depth and orientation of defects and to confirm the present findings of damage resulting from direct interaction with the electron beam.

3. Results

3.1. Equilibrium vacancy concentrations at elevated temperature

Fig. 1 describes schematically how spatial maps, such as those shown in Fig. 4, are generated by way of 4D-STEM strain mapping technique to capture local changes in lattice parameter (indicated by the color-coded lattice parameter values) within the Au thin film. Recurring measurements were acquired in situ at sample regions R1 – R4 (red boxes in Fig. 1a) during each temperature step (example test data presented in Fig. 2). Fig. 4 compares the initial 17 °C (a) measurement to the high temperature scans of the same region after heat treatment (800 °C (b) and 1000 °C (c)). The maps exhibit thermally induced lattice expansion (1.23% and 1.60% respectively) that is consistent across the four scan regions (assuming isotropic expansion). For example, the 1000 °C scan is a uniformly darker shade of blue compared to the 800 °C scan and corresponds to the maximum observed lattice parameter of 4.136 (0.002) Å at the peak aged condition (1000 °C) just below the melting point (1063 °C) of pure Au. This is in agreement (< 1% error) with recent reporting of XRD measurement (4.14703(4) Å) on bulk single crystal Au at 1000 °C [30]. Rapid cooling of the sample (enabled by thermo-electric MEMS device) transpires in ~ 1 milli-seconds, similar to previous studies involving quenching (10^6 deg/sec) of bulk crystal [28,29,38]. Overall, the microstructure remained consistent throughout the heating and cooling experiments, with minimal discernable changes in microstructural imperfections or features such as twins, stacking faults and voids. Local fluctuations in strain associated with vacancies accumulated over the heating cycle were not resolvable in the HAADF-STEM images or the spatial maps due to the ~1 nm minimum probe size. The interaction volume at each probe position is equivalent to the film thickness. Furthermore, there are no indications of heterogeneous defect formation or coarsening after multiple heating cycles. The resulting lattice parameter decreases to 4.072(0.001) Å after cooling (Fig. 4d), comparable to measurement of the pre-heated condition, although not fully, and the discrepancy is resolved later.

Fig. 5 combines the lattice expansion Δa/a from values collected at 17 °C (initial strain value used as a reference), 800 °C and 1000 °C that are averaged over the four sample regions (R1 – R4). Similarly, the average measured length expansion ΔL/L was extracted from careful measurement of the minimum dimension of these bridge-like features (between adjacent holes in the film) from HR-STEM images (Fig. 2a-d) acquired at each temperature / time step. Both measurements are plotted with respect to temperature and trendlines are fitted to each

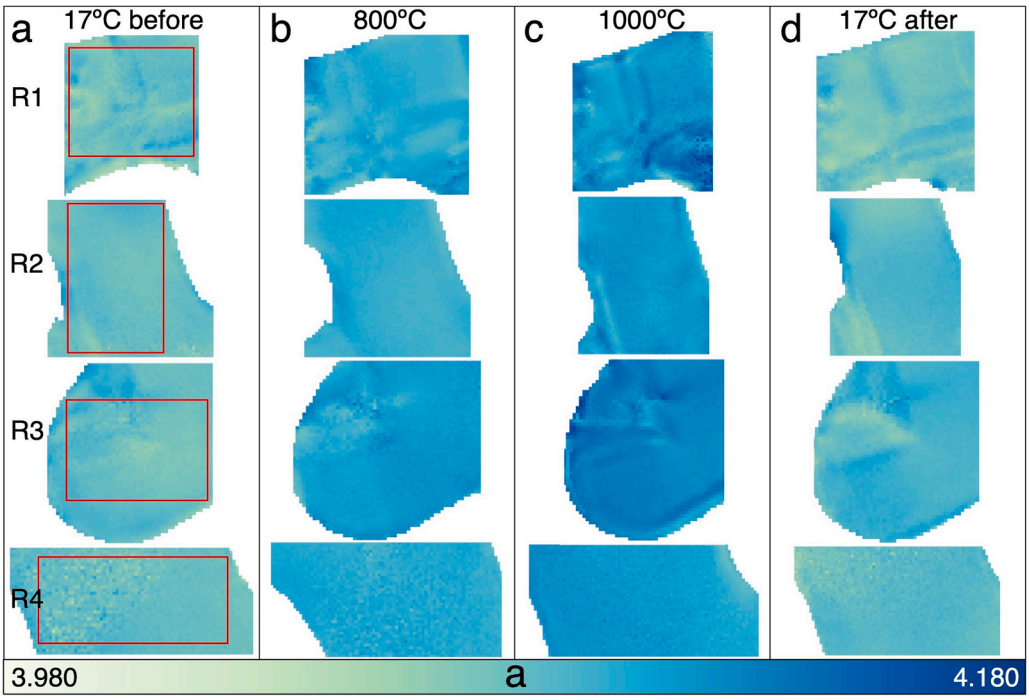

Fig. 4. 4D-STEM lattice parameter mapping of thermally annealed Au. Four regions of interest are specified as R1 – R4, corresponding to the red boxes shown in Fig. 1(a). The average lattice parameter taken from scan positions in the red boxes in (a) is used as a reference to subsequent data sets taken from the same location. (a) 17 °C before heat treatment. (b) 800 °C during heat treatment. (c) 1000 °C during heat treatment. (d) 17 °C after rapidly cooling. (For interpretation of the references to colour in this figure legend, the reader is referred to the web version of this article.)

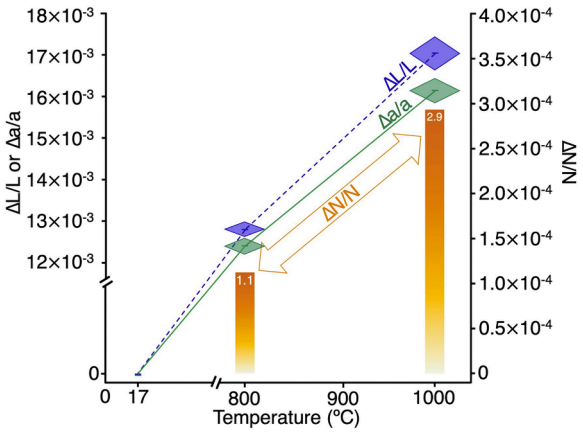

Fig. 5. Length expansion (blue) and lattice parameter expansion (green) of the pure Au thin film with respect to temperature (truncated to visualize measurements taken close to the melting point). Net added concentration of vacancies (ΔN/N noted by secondary vertical axis) is indicated (yellow / orange) for measurements taken at elevated temperature. All measurements include standard deviation (y-axis) for statistical comparison and the temperatures reported are within the 5% accuracy for the in situ heating device. (For interpretation of the references to colour in this figure legend, the reader is referred to the web version of this article.)

dataset to illustrate the separation between the two measured variables with temperature. Previous work shows this divergence from linear thermal expansion becomes most noticeable while annealing temperatures approach the melting point (650 – 1063 °C) and the temperature range is presented accordingly from 700 – 1000 °C (peak aging temperature). This observed separation shares a direct relation with an increasing concentration of point defects [10] as indicated by the orange bars plotted with respect to the secondary vertical axis (ΔN/N). The larger change in sample dimension than lattice parameter indicates the measurements are detecting additional lattice sites, which are produced by forming vacancy defects and displacing those atoms to new sites on the surfaces. However, this is the first reported case where these trends (previously only performed with X-rays on a bulk crystal) are coupled with direct microstructural observations.

3.2. Retained vacancies in thermally cycled Au

Short (~minutes) and long (~days) timescales at room temperature (17 °C) and the retention of vacancy defects was explored by comparing lattice parameter maps acquired at the same sample location (R2 in Fig. 1a). The measurements were taken during two identical heating experiments (single cycle timescale presented in Fig. 6a) which took place 30 days apart. The data presented in Fig. 6b plots the lattice parameter change and with respect the number thermal cycles. The long-term rest period at room temperature, indicated by the vertical dashed line, resulted in a lattice expansion of $0.29 \times 10^{-3}(0.26)$ compared to the initial measurement, which is an 80% reduction compared to $1.45 \times 10^{-3}(0.41)$ measured after the fourth cycle of the first experiment. Moreover, the normalized linear dilation of the sample region decreased by 133% from $3.26 \times 10^{-3}(0.12)$ to $1.11 \times 10^{-3}(0.10)$ after the 30-day rest which was followed by a 175% climb to $3.59 \times 10^{-3}(0.16)$ after four additional cycles.

Interestingly, over both short and long timescales, complete lattice relaxation did not occur after each heating-cooling cycle as shown in Fig. 6b where measurements of the same location were taken approximately eight minutes apart (time between measurements in a single cycle outlined in Fig. 6a) or after a period of 30 days (stored in air at ambient temperature). There is a notable increase in lattice parameter and linear dilation with the number of heating/cooling cycles. Once brought up to temperature, the vacancies establish equilibrium within a millisecond or less. When quenched to room temperature, the vacancies will be retained in the sample for a period of roughly 1 hour before beginning to escape to the surface. After 12-hours at 17 °C, defects are expected to deplete to concentrations $\leq 1.0 \times 10^{-6}$ which is below the resolution of our current measurement capabilities. When heated to 1000 °C, one would expect substantial diffusional creep under the influence of surface tension due to the large surface to volume ratio. The change in shape and lattice parameter after 30-days at room temperature shows the amount the material had crept at temperature, with that plastic deformation being largely retained when cooled back to 17 °C (in

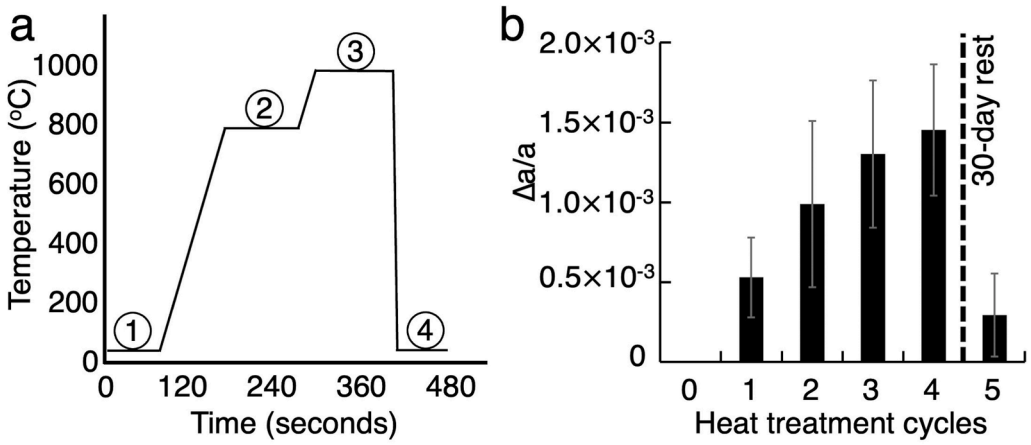

Fig. 6. Heating cycle for in situ thermal cycling experiment. (a) Temperature vs. time plot of a single heat treatment cycle. Heat treatment cycle consists of heating of ~10 °C/*sec* interrupted by holds at 800 °C and 1000 °C (peak temperature) for 4D-STEM data collection and followed by rapid cooling (~106 °C/*sec*). 4D-STEM datasets collected at 4 indicated time intervals. (b) This process was repeated over several heat treatment cycles where mean lattice expansion (reference taken before first heating cycle) and standard deviation is plotted via measurements taken at 17 °C (step 4 of (a)) after each heating cycle.

contrast to the residual vacancy population, which anneals out over this time). This leaves a large change in linear dilation, and a slight residual stress would explain the more modest lattice expansion. Considering the near-zero defect concentration after 30-days at room temperature, the creep relaxation and residual strain are the sole contributors to lattice expansion and linear dilation after this time. By normalizing this contribution to the measurements taken at the four heating cycle conditions, the vacancy concentration ($\sim 2 \times 10^{-4} - 3 \times 10^{-4}$)) and relaxation volume (reduced by 0.3 – 0.5 atomic volumes) are directly measured (Fig. 7). Furthermore, the normalized measurement suggesting defects are largely retained in the short-term after four heating cycles is in alignment with the asymmetric behavior of defects upon heating (rapid accumulation) and cooling (slow depletion).

3.3. Point defects created by knock-on electron beam damaged in Al

The above discussion shows how we can measure the vacancy content in model equilibrated samples ideally suited to measure both local lattice and volume expansion. However, it is not necessary to have a holey film sample to apply this technique. For example, we measured the formation and evolution of non-equilibrium defects and demonstrated the mapping technique to defects accumulated in an electropolished Al sample by creating highly localized irradiation damage via the condensed 300 kV electron beam scanned at regular time intervals (60 – 120 s). This is equivalent to years of radiation exposure in practical engineering systems such as nuclear reactors, however, electron irradiation ($\sim 10^{-4} - 10^{-3}$ dpa/s) produces much higher dose rates compared to neutron irradiation ($\sim 10^{-7}$ dpa/s) [39]. The knock-on electron beam damage method is applied to $a \leq 100$ nm^2 square sample area (red boxes in Fig. 8) while 4D-STEM datasets were acquired for 12 consecutive scans (Fig. 9). Qualitative changes were observed after each scan that primarily consisted of heterogeneous irradiation defects.

Fig. 10a highlights the changes in diffraction contrast resulting from damage accumulation and the sequential lattice parameter maps suggest interstitial clusters that are identified by light green colored strain fields (Fig. 10b) on the order of 5 – 20 nm. The average lattice parameter associated with these electron irradiation-induced defect clusters is consistently lower than the global average lattice parameter of 4.048 (0.001) Å which suggests these are comprised of interstitial-type defects, where the outward pressure e.g., a split interstitial structure (see Fig. 1b) causes a compressive stress state on the surrounding lattice. Accumulation of vacancies is expected in conjunction with interstitial cluster growth. However, the volume of an interstitial is typically greater in magnitude than that of a vacancy, consistent with the compressive net effect in the measurement. In the ultrathin ($\leq$ 50 nm) electropolished sample, we posit that the un-irradiated sample volume surrounding the scan region imposes volumetric constraints on the irradiated volume and we can assume that $\Delta L/L$ is essentially zero. The reduction in lattice parameter coincides with an increase in point defect concentration ($\Delta N/N$), in the form of split interstitials and vacancies, with respect to the increase in number of 4D-STEM scans as shown in Fig. 10c, reaching a plateau after ~ 10 scans.

4. Discussion

Beyond the improvement in spatial resolution that our method has demonstrated for detecting changes in nano-scale defect concentration, such as homogenous vacancies in thermally cycled Au and heterogeneous interstitial defects in irradiated Al, our measurements provide direct insight into the migration of point defects in a spatially resolved manner. First, given the retention of vacancies upon cooling and the minimal heterogeneous defects retained after each ~ 480 second cycle, we can estimate the migration energy of vacancies in Au using the minimum dimension (thickness) of the Au thin film. Previous estimates of the migration energy in Au have shown a large discrepancy [40], to the point that it was not clear if we would be able to retain any vacancies

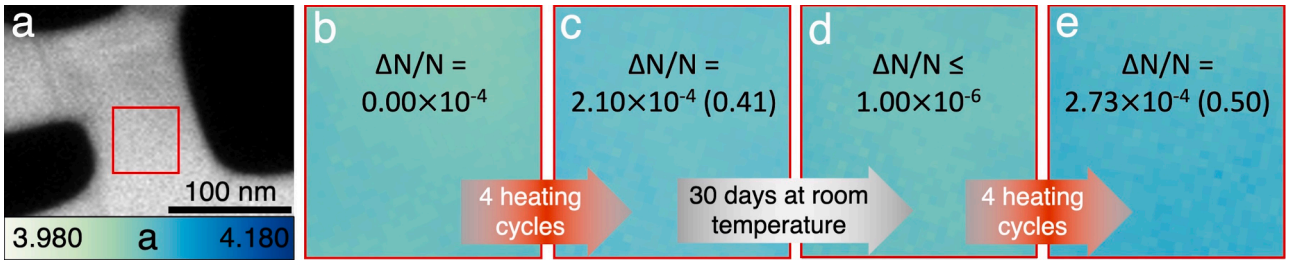

Fig. 7. 4D-STEM lattice parameter mapping of Au post-quenching. (a) HAADF-STEM micrograph of the second sample location (R2). Room temperature 4D-STEM lattice parameter maps taken (b) reference lattice at R2 immediately before, (c) immediately after four heating cycles, (d) 30 days after first experiment and (e) after a four additional heating cycles. The label on each map indicates net added vacancy concentration and standard deviation over the field of view.

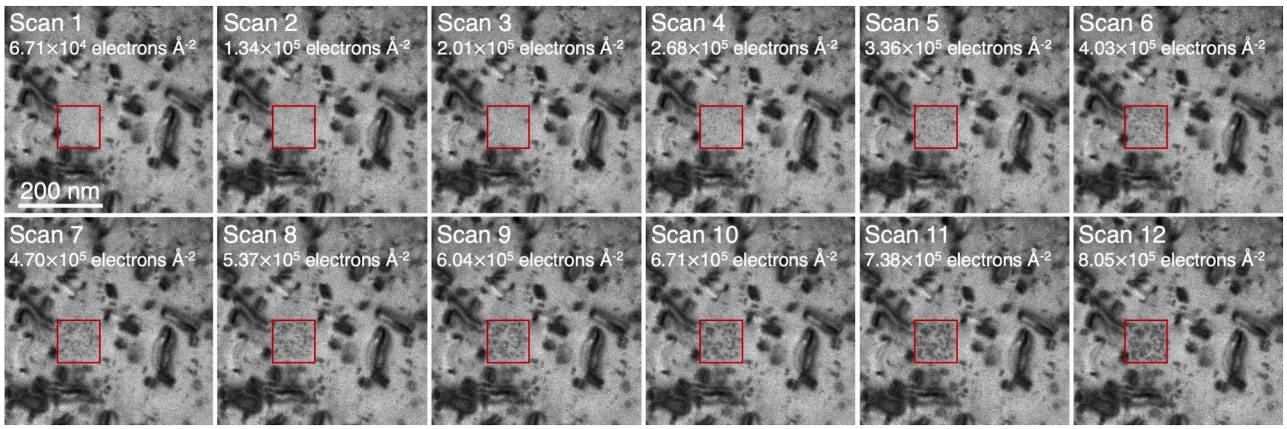

Fig. 8. ADF-STEM image data for knock-on electron beam damage experiment. Images of Al sample exposed to 300 kV electron beam irradiation were taken during collection of consecutive 4D-STEM scans. Red boxes indicate electron irradiation exposed region where 4D-STEM scan is taken. Total dose in electrons $\mathring{A}^{-2}$ is provided for each scan. (For interpretation of the references to colour in this figure legend, the reader is referred to the web version of this article.)

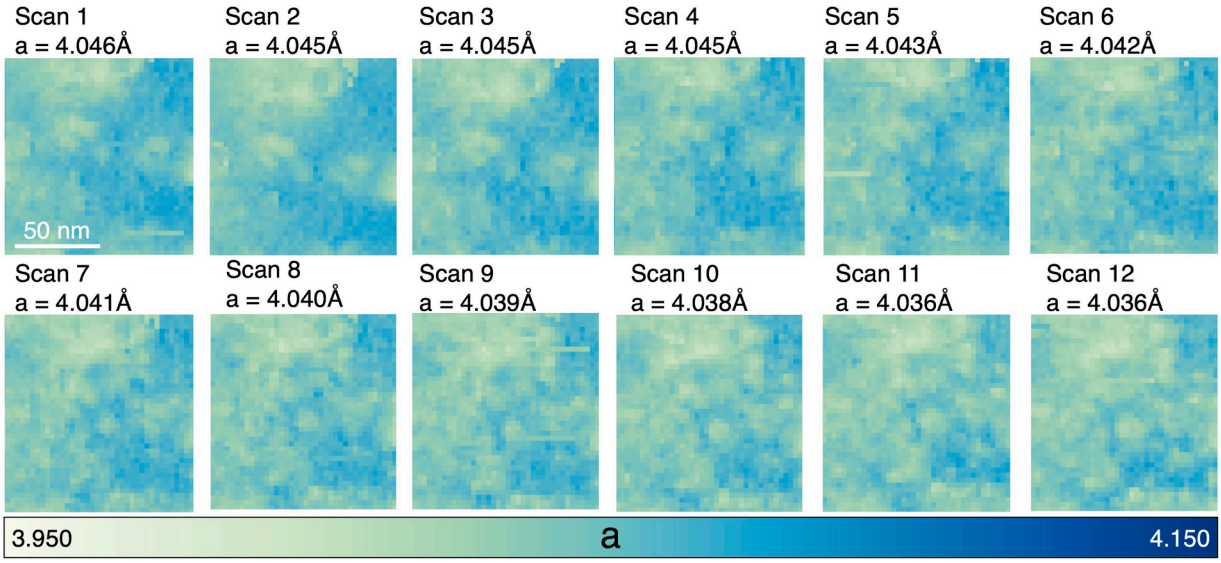

Fig. 9. Sample 4D-STEM data for knock-on electron beam damage experiment. Lattice parameter maps generated from Al sample exposed to 300 kV electron beam irradiation during collection of consecutive 4D-STEM scans. Qualitative maps track the nucleation and growth of several prominent point defect clusters (light green). (For interpretation of the references to colour in this figure legend, the reader is referred to the web version of this article.)

in our quenched thin films for the minute long dwell period between rapid cooling and acquiring 4D-STEM scans. The migration of point defects for 3-dimensional random walk motion can be described via $r = d\sqrt{\mathrm{n}}$ [40]. "d" is the nearest neighbor hop distance 2.9 Å and "n" is the total number of hops: $n = k \times \mathrm{t(seconds)}$ where "k" is the rate of hops. $k = \mathrm{N}\nu \times \exp\left(-\frac{\mathrm{E_m}}{\mathrm{k_b T}}\right)$ is a function of the migration energy ($\mathrm{E_m}$), the value of which has been reported by several independent studies on Au. Matsukawa et al. reported $\mathrm{E_m} = 0.85$ eV which results in little to no movement in the system [40]. Contradictory evidence reports $\mathrm{E_m}$ as low as 0.62 eV, resulting in movement of several hundred nanometers, much larger than the distance required for a defect to escape from nearby surfaces of our thin films ($\leq$ 25 nm). The energy range for pure Al is reported at 0.58 eV – 0.71 eV [41]. Our results indicate that the migration energy to retain point defects is much closer to the Matsukawa findings in Au and 0.66 eV reported in Al [41] suggesting next to no defect movement considering the defects in both samples are retained during the room temperature dwell period between cycles (thermal or irradiation) in our experiments. Furthermore, retention of vacancy defects in the Au thin film is more apparent after multiple heating cycles as shown in Fig. 7b. This change is several orders of magnitude higher than theoretical contributions from point defects, suggesting that other mechanisms discussed such as lattice diffusion creep [5,42,43] and residual stress contributions are likely at play.

The 4D-STEM characterization method provides a robust qualitative description of the microstructure within a wide field of view and nanoscale resolution which makes it ideally suited to capturing heterogeneous point defect distributions. For example, the Au showed no indications of heterogeneous defect formation as the lattice parameter maps describe a microstructure containing mono vacancies, randomly dispersed throughout the thin film that undergo no apparent coarsening after multiple heating cycles. Pre-existing defects in the HAADF-STEM images and reconstructed 4D-STEM lattice parameter maps (Fig. 4) Show no formation or growth of voids that may be indicate equilibrium vacancies migrating to defect sinks and. Therefore, the high temperature lattice parameter measured is a close match to XRD-based lattice parameter measurement of bulk crystal [30].

The fundamental difference between the equilibrium behavior in Au and the non-equilibrium behavior in Al can be observed in the formation of defect clusters. In the irradiated regions of the pure Al sample,

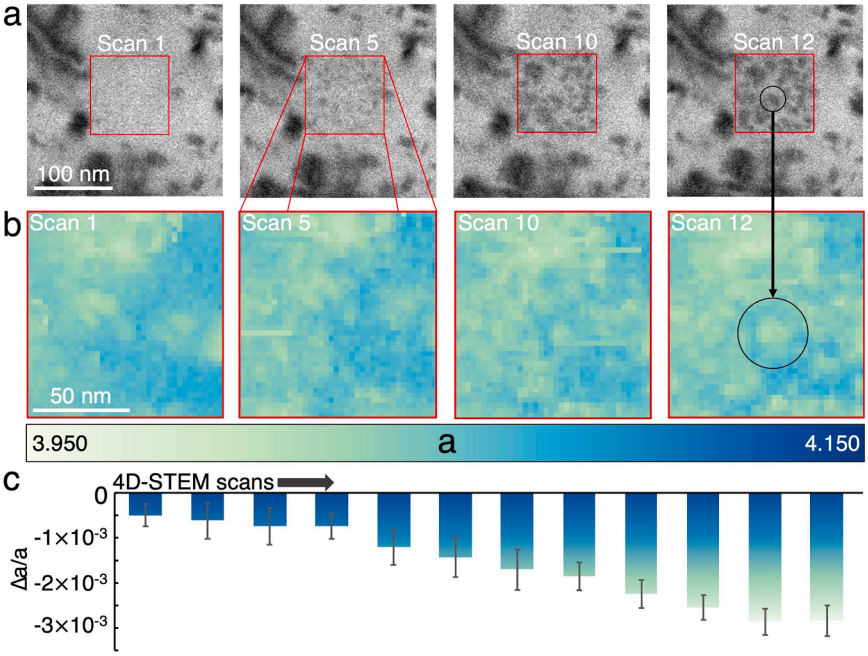

Fig. 10. 4D-STEM defect accumulation in pure Al under direct electron beam exposure. (a) HR-ADF-STEM images and lattice parameter maps of 4D-STEM scans taken within the corresponding red boxes. (b) 4D-STEM lattice parameter maps of data taken from red scan boxes in (a). Nanoscale irradiation defects are generated by direct exposure to condensed STEM probe. Black circles in Scan 12 indicate a prominent defect cluster formed during irradiation. (c) Lattice expansion and standard deviation over the field of view is plotted with respect to number of 4D-STEM scans (67,100 electrons$Å^{-2}$ per 4D-STEM scan). (For interpretation of the references to colour in this figure legend, the reader is referred to the web version of this article.)

multiple passes of the condensed nanoprobe electron beam causes controlled formation of defect clusters that grow to 5 – 20 nm as shown in Fig. 10. The readiness for visible clusters to develop rather than remain evenly dispersed as mono-defects indicates they are mobile interstitials in the Al sample that diffuse and coalesce. As individual defects agglomerate, they coarsen and, due to the size and the strains imposed on the neighboring atoms, act like sinks that attract interstitials that would otherwise escape the irradiated zone. Critically, when interstitials migrate to the clustered defects, they recombine with single vacancies located at the perimeter of the cluster and occupy that lattice position, annihilating both defects in the process. As the accumulation of vacancies and recombination with interstitials repeats over several exposures to the electron beam, quasi-steady-state is reached, and defect cluster growth becomes stagnant [44–47].

5. Summary and conclusions

In conclusion, we demonstrated a method to map the concentrations of both equilibrium and non-equilibrium vacancy defects with nanometer spatial resolution and rapid time resolution. Similar to the classical work by Simmons and Balluffi [9–11], our method is generally-applicable in that all that is required are independent measurements of dilation and lattice parameters. In lieu of linear dilation, one could use computational models to correlate the lattice parameter change to vacancy concentration. In our case, the spatial resolution of the 4D-STEM also provides the ability to measure heterogeneous vacancy or interstitial concentrations, such as that shown in our irradiated regions of Al. Through this method, we experimentally benchmarked the migration energy of point defects in Au and compared equilibrium behavior to non-equilibrium super-saturations. We expect this methodology to be applied to basic and applied science applications in the future, mapping vacancy concentrations in transforming materials such as battery cathode materials and in materials subjected to extreme environments of temperature, stress, and irradiation.

CRediT authorship contribution statement

Sean H. Mills: Writing – review & editing, Writing – original draft, Visualization, Investigation, Methodology, Conceptualization. **Steven E. Zeltmann:** Visualization. **Peter Ercius:** Writing – review & editing, Investigation. **Aaron A. Kohnert:** Writing – review & editing, Visualization. **Blas P. Uberuaga:** Writing – review & editing, Project administration, Funding acquisition, Visualization. **Andrew M. Minor:** Conceptualization, Methodology, Funding acquisition, Project administration, Supervision, Writing – original draft, Writing – review & editing.

Declaration of Competing Interest

The authors declare that they have no competing financial interests or personal relationships that could have appeared to influence the work reported in this paper.

Data availability

: The raw data required to reproduce these findings are available to download from Zenodo (DOI: 10.5281/zenodo.7041997) and upon reasonable request to the corresponding author.

Acknowledgments

Primary support and funding for this work came from FUTURE (Fundamental Understanding of Transport Under Reactor Extremes), an Energy Frontier Research Center funded by the U.S. Department of Energy, Office of Science, Basic Energy Sciences. Work at the Molecular Foundry was supported by the Office of Science, Office of Basic Energy Sciences, of the U.S. Department of Energy under Contract No. DE-AC02–05CH11231. S.E. Zeltmann was supported by STROBE, a National Science Foundation STC funded under grant no. DMR 1548924.

References

[1] J. Frenkel, Über die Wärmebewegung in festen und flüssigen Körpern, Z. Med. Phys. 35 (1926) 652–669.
[2] J. Silcox, P. Hirsch, Direct observations of defects in quenched gold, Philos. Mag. 4 (1959) 72–89.
[3] J.P. Hirth, J. Lothe, T. Mura, Theory of dislocations, J. Appl. Mech. 50 (1983), 476.
[4] M. Kassner, P. Kumar, W. Blum, Harper–dorn creep, Int. J. Plast. 23 (2007) 980–1000.
[5] F. Nabarro, Steady-state diffusional creep, Philos. Mag. 16 (1967) 231–237.

[6] R.W. Grimes, R.J. Konings, L. Edwards, Greater tolerance for nuclear materials, Nat. Mater. 7 (2008) 683–685.
[7] W. Zhou, Y. Yang, G. Zheng, K.B. Woller, P.W. Stahle, A.M. Minor, M.P. Short, Proton irradiation-decelerated intergranular corrosion of Ni-Cr alloys in molten salt, Nat. Commun. 11 (2020) 1–7.
[8] Y. Kraftmakher, Equilibrium vacancies and thermophysical properties of metals, Phys. Rep. 299 (1998) 79–188.
[9] R. 0 Simmons, R.W. Balluffi, Measurements of equilibrium vacancy concentrations in aluminum, Phys. Rev. 117 (1960), 52.
[10] R.O. Simmons, R.W. Balluffi, Measurement of equilibrium concentrations of lattice vacancies in gold, Phys. Rev. 125 (1962), 862.
[11] R.O. Simmons, R.W. Balluffi, Measurement of equilibrium concentrations of vacancies in copper, Phys. Rev. 129 (1963), 1533.
[12] R. West, Positron Studies of Lattice Defects in metals, in: Positrons in Solids, Springer, 1979, pp. 89–144.
[13] C. Hugenschmidt, Positrons in surface physics, Sci Rep 71 (2016) 547–594.
[14] F. Selim, Positron annihilation spectroscopy of defects in nuclear and irradiated materials-a review, Mater. Charact. 174 (2021), 110952.
[15] C. Ophus, Four-dimensional scanning transmission electron microscopy (4D-STEM): from scanning nanodiffraction to ptychography and beyond, Microsc. Microanal. 25 (2019) 563–582.
[16] B.H. Savitzky, S.E. Zeltmann, L.A. Hughes, H.G. Brown, S. Zhao, P.M. Pelz, T. C. Pekin, E.S. Barnard, J. Donohue, L.R. DaCosta, others, py4DSTEM: a software package for four-dimensional scanning transmission electron microscopy data analysis, Microsc. Microanal. 27 (2021) 712–743.
[17] S.E. Zeltmann, A. Müller, K.C. Bustillo, B. Savitzky, L. Hughes, A.M. Minor, C. Ophus, Patterned probes for high precision 4D-STEM bragg measurements, Ultramicroscopy 209 (2020), 112890.
[18] V. Ozdol, C. Gammer, X. Jin, P. Ercius, C. Ophus, J. Ciston, A. Minor, Strain mapping at nanometer resolution using advanced nano-beam electron diffraction, Appl. Phys. Lett. 106 (2015), 253107.
[19] M.J. Hÿtch, A.M. Minor, Observing and measuring strain in nanostructures and devices with transmission electron microscopy, MRS Bull. 39 (2014) 138–146, https://doi.org/10.1557/mrs.2014.4.
[20] Y. Ding, Y. Choi, Y. Chen, K.C. Pradel, M. Liu, Z.L. Wang, Quantitative nanoscale tracking of oxygen vacancy diffusion inside single ceria grains by in situ transmission electron microscopy, Mater. Today 38 (2020) 24–34.
[21] Y. Yang, W. Zhou, S. Yin, S. Wang, Q. Yu, R. Ritchie, M. Asta, J. Li, M. Short, A. Minor, 4D-STEM Imaging of nanostructural heterogeneities in Ni-20Cr after corrosion in molten salt, Microsc. Microanal. 27 (2021) 2134–2135.
[22] Y. Yang, W. Zhou, S. Yin, S.Y. Wang, Q. Yu, M.J. Olszta, Y.-.Q. Zhang, S.E. Zeltmann, M. Li, M. Jin, others, One dimensional wormhole corrosion in metals, ArXiv Preprint ArXiv:2203.16312. (2022).
[23] J. Vancea, G. Reiss, F. Schneider, K. Bauer, H. Hoffmann, Substrate effects on the surface topography of evaporated gold films—A scanning tunnelling microscopy investigation, Stem Cells Int. 218 (1989) 108–126.
[24] F. Niekiel, S.M. Kraschewski, J. Müller, B. Butz, E. Spiecker, Local temperature measurement in TEM by parallel beam electron diffraction, Ultramicroscopy 176 (2017) 161–169.
[25] J. Lloyd, S. Nakahara, On the diffusion of excess vacancies to free surfaces and voids in thin films, J. Electrochem. Soc. 125 (1978), 2037.
[26] R. Wittmann, C. Parzinger, D. Gerthsen, Quantitative determination of lattice parameters from CBED patterns: accuracy and performance, Ultramicroscopy 70 (1998) 145–159.
[27] T. Kino, J.S. Koehler, Vacancies and divacancies in quenched gold, Phys. Rev. 162 (1967), 632.
[28] J.A. Ytterhus, R.W. Balluffi, On the annealing of quenched-in vacancies in gold, Philos. Mag. 11 (1965) 707–727, https://doi.org/10.1080/14786436508230078.
[29] J.W. Kauffman, Quenching-in of lattice vacancies in pure gold, Phys. Rev. 97 (1955), 555.
[30] M.G. Pamato, I.G. Wood, D.P. Dobson, S.A. Hunt, L. Vočadlo, The thermal expansion of gold: point defect concentrations and pre-melting in a face-centred cubic metal, J. Appl. Crystallogr. 51 (2018) 470–480.
[31] R. Dou, B. Derby, Deformation mechanisms in gold nanowires and nanoporous gold, Philos. Mag. 91 (2011) 1070–1083.
[32] P. Horodek, Positron annihilation studies of irradiation-induced defects with swift heavy ions in gold, Vacuum 164 (2019) 421–427, https://doi.org/10.1016/j.vacuum.2019.03.056.
[33] K.C. Bustillo, S.E. Zeltmann, M. Chen, J. Donohue, J. Ciston, C. Ophus, A.M. Minor, 4D-STEM of Beam-Sensitive Materials, Acc. Chem. Res. 54 (2021) 2543–2551.
[34] P. Liu, Measurement of vacancy migration energy by using HVEM. Fusion Energy, IntechOpen, 2019, p. 103.
[35] D.A. Muller, J. Silcox, Radiation damage of Ni3Al by 100 keV electrons, Philos. Mag. A 71 (1995) 1375–1387.
[36] T. Bullough, Sputtering and the formation of nanometre voids and holes in aluminium in a scanning transmission electron microscope, Philos. Mag. A 75 (1997) 69–85.
[37] B.F. McEwen, K.H. Downing, R.M. Glaeser, The relevance of dose-fractionation in tomography of radiation-sensitive specimens, Ultramicroscopy 60 (1995) 357–373.
[38] W. Desorbo, Calorimetric studies on annealing quenched-in defects in gold, Phys. Rev. 117 (1960) 444.
[39] C. Karthik, J. Kane, D.P. Butt, W. Windes, R. Ubic, In situ transmission electron microscopy of electron-beam induced damage process in nuclear grade graphite, J. Nucl. Mater. 412 (2011) 321–326.
[40] Y. Matsukawa, S.J. Zinkle, One-dimensional fast migration of vacancy clusters in metals, Science 318 (2007) 959–962.
[41] K. Ono, T. Kino, Migration energy of mono-vacancy in aluminum at high temperature, J. Phys. Soc. Jpn. 44 (1978) 875–881.
[42] F. Nabarro, others, Report of a Conference on the Strength of Solids, The Physical Society, London., 1948, p. 590, 75.
[43] H. Conyers, Diffusional viscosity of a polycrystalline solid, J. Appl. Phys. 21 (1950) 437–445.
[44] H. Wiedersich, Evolution of defect cluster distributions during irradiation. Materials Science Forum, Trans Tech Publ, 1992, pp. 59–74.
[45] L. Rehn, H. Wiedersich, Freely-migrating defects: their production and interaction with cascade remnants. Materials Science Forum, Trans Tech Publ, 1992, pp. 43–58.
[46] S. Zinkle, B. Singh, Analysis of displacement damage and defect production under cascade damage conditions, J. Nucl. Mater. 199 (1993) 173–191.
[47] S.J. Zinkle, K. Farrell, Void swelling and defect cluster formation in reactor-irradiated copper, J. Nucl. Mater. 168 (1989) 262–267.